Energy Materials and Devices

Open Access
Research Article

Graphical Abstract

Asymmetric quasi-solid-state composite electrolytes via self-assembly of molecular brushes and hairy nanoparticles for dendrite-free lithium metal batteries

Shenghao Lin[1], Yin Cui[1] ✉, Guofang Yu[1], Dongtian Miao[1], Ruliang Liu[2], and Dingcai Wu[1] ✉

[1] *PCFM Lab and GDHPRC Lab, School of Chemistry, Sun Yat-sen University, Guangzhou 510006, China*
[2] *School of Chemistry and Materials Science, Guangdong University of Education, Guangzhou 510303, China*

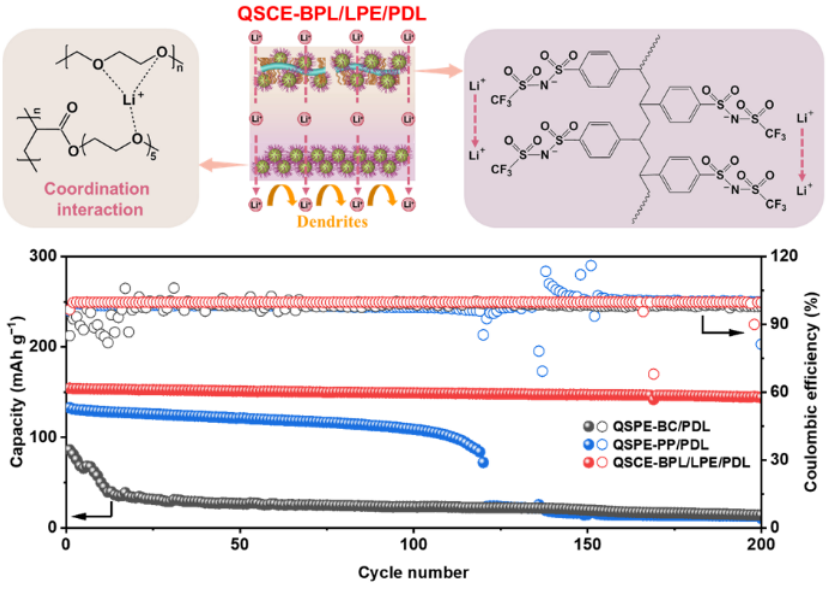

In this study, an asymmetric quasi-solid-state composite electrolyte (QSCE-BPL/LPE/PDL) was constructed by evaporation-induced self-assembly of 1D molecular brushes and 0D hairy ceramic nanoparticles, followed by *in situ* polymerization. The resulting ultrathin QSCE-BPL/LPE/PDL (19 μm) delivers a high ionic conductivity of 5.44 × 10^{-4} S cm^{-1} and a Li^+ transference number of 0.67, and enables Li/$LiFePO_4$ cells to operate for 200 cycles with 94% capacity retention at 0.5 C.

✉ Address correspondence to
Yin Cui, cuiyin1@sztu.edu.cn;
Dingcai Wu, wudc@mail.sysu.edu.cn

Received: April 11, 2026
Revised: April 23, 2026
Accepted: April 24, 2026

9370095

Read Online

Citation: Lin S., Cui Y., Yu G., et al. Asymmetric quasi-solid-state composite electrolytes via self-assembly of molecular brushes and hairy nanoparticles for dendrite-free lithium metal batteries. *Energy Mater. Devices*, 2026, 4(2), 9370095. https://doi.org/10.26599/EMD.2026.9370095

Energy Materials and Devices
https://doi.org/10.26599/EMD.2026.9370095
Open Access
Research Article

Asymmetric quasi-solid-state composite electrolytes via self-assembly of molecular brushes and hairy nanoparticles for dendrite-free lithium metal batteries

Shenghao Lin[1], Yin Cui[1] ✉, Guofang Yu[1], Dongtian Miao[1], Ruliang Liu[2], and Dingcai Wu[1] ✉

[1] *PCFM Lab and GDHPRC Lab, School of Chemistry, Sun Yat-sen University, Guangzhou 510006, China*
[2] *School of Chemistry and Materials Science, Guangdong University of Education, Guangzhou 510303, China*

Cite this article: *Energy Mater. Devices* 2026, **4**(2): 9370095. https://doi.org/10.26599/EMD.2026.9370095

ABSTRACT

The practical application of lithium metal batteries is severely hindered by flammable liquid electrolytes and uncontrollable lithium dendrite growth. In this study, we propose a novel asymmetric quasi-solid-state composite electrolyte (denoted as QSCE-BPL/LPE/PDL) designed to overcome these challenges. QSCE-BPL/LPE/PDL is fabricated by evaporation-induced self-assembly of one-dimensional molecular brush BC-*g*-PLiSTFSI [BC = bacterial cellulose, PLiSTFSI = poly(lithium 4-styrenesulfonyl-(trifluoromethylsulfonyl) imide)] and zero-dimensional hairy nanoparticle LL-*g*-PEGMA [LL = $Li_{6.4}La_3Zr_{1.4}Ta_{0.6}O_{12}$, PEGMA = poly(oligo(ethylene glycol) methyl ether methacrylate)], followed by *in situ* cationic ring-opening polymerization of 1,3-dioxolane. The resulting ultrathin QSCE-BPL/LPE/PDL (19 μm) possesses a unique asymmetric architecture comprising a rigid layer of hairy nanoparticles to suppress dendrite penetration and a composite layer to ensure good interfacial contact with the cathode. The grafted PLiSTFSI side chains enable single Li^+ conduction to reduce concentration polarization, and the PEGMA side chains promote lithium salt dissociation to accelerate Li^+ transport. This design yields a three-dimensional porous network that provides continuous and fast Li^+ transport pathways. The optimized electrolyte achieves a high ionic conductivity of 5.44 × 10^{-4} S cm^{-1} and a Li^+ transference number of 0.67 at room temperature. Consequently, Li/$LiFePO_4$ cells with QSCE-BPL/LPE/PDL can operate stably for 200 cycles with a high-capacity retention of 94% at 0.5 C. This study provides a feasible molecular engineering strategy for developing high-performance and safe lithium metal batteries.

KEYWORDS

quasi-solid-state composite electrolyte, molecular brush, hairy nanoparticle, lithium metal battery

1 Introduction

With the development of electric vehicles and smart grids, there is a growing demand for battery safety and energy density that cannot be satisfied by traditional lithium-ion batteries[1,2]. The replacement of the common graphite anode with lithium metal, which possesses an extremely high theoretical specific capacity (3860 mAh g^{-1}) and a low electrochemical potential (−3.04 V vs. the standard hydrogen electrode), has attracted extensive attention[3,4]. The development of next-generation and high-energy-density lithium metal batteries (LMBs) is considered critical; however, LMBs are prone to serious safety issues due to flammable organic solvents and harmful lithium dendrites[5–9].

Compared with existing liquid electrolytes (LEs), solid-state electrolytes (SEs) with high mechanical strength and lithium-ion (Li^+) conductivity are promising materials to address the safety hazards and energy density issues of LMBs[10,11]. In general, SEs can be categorized into solid-state polymer electrolytes (SPEs), inorganic ceramic electrolytes (ICEs), and solid-state composite electrolytes (SCEs)[12]. By adding inorganic ceramic components into a polymer/lithium salt matrix, SCEs combine the advantages of ICEs and SPEs and have become promising electrolyte systems for solid-state LMBs[13–16]. However, because the preparation method of traditional SCEs is based on simple mechanical mixing, SCEs still face various challenges, such as the poor interfacial compatibility between different functional components, low ionic conductivity at room temperature, and difficulty in completely inhibiting the growth of lithium dendrites, which severely restrict the application of SCEs in LMBs (Fig. 1a).

Recently, as an important type of SCEs, asymmetric quasi-solid-state composite electrolytes (QSCEs) have attracted extensive attention because of their distinctive multilayer architectures, which enable function customization based on the cathode and anode requirements[17,18].

Received: April 11, 2026 / **Revised:** April 23, 2026 / **Accepted:** April 24, 2026

✉**Address correspondence to** Yin Cui, cuiyin1@sztu.edu.cn; Dingcai Wu, wudc@mail.sysu.edu.cn

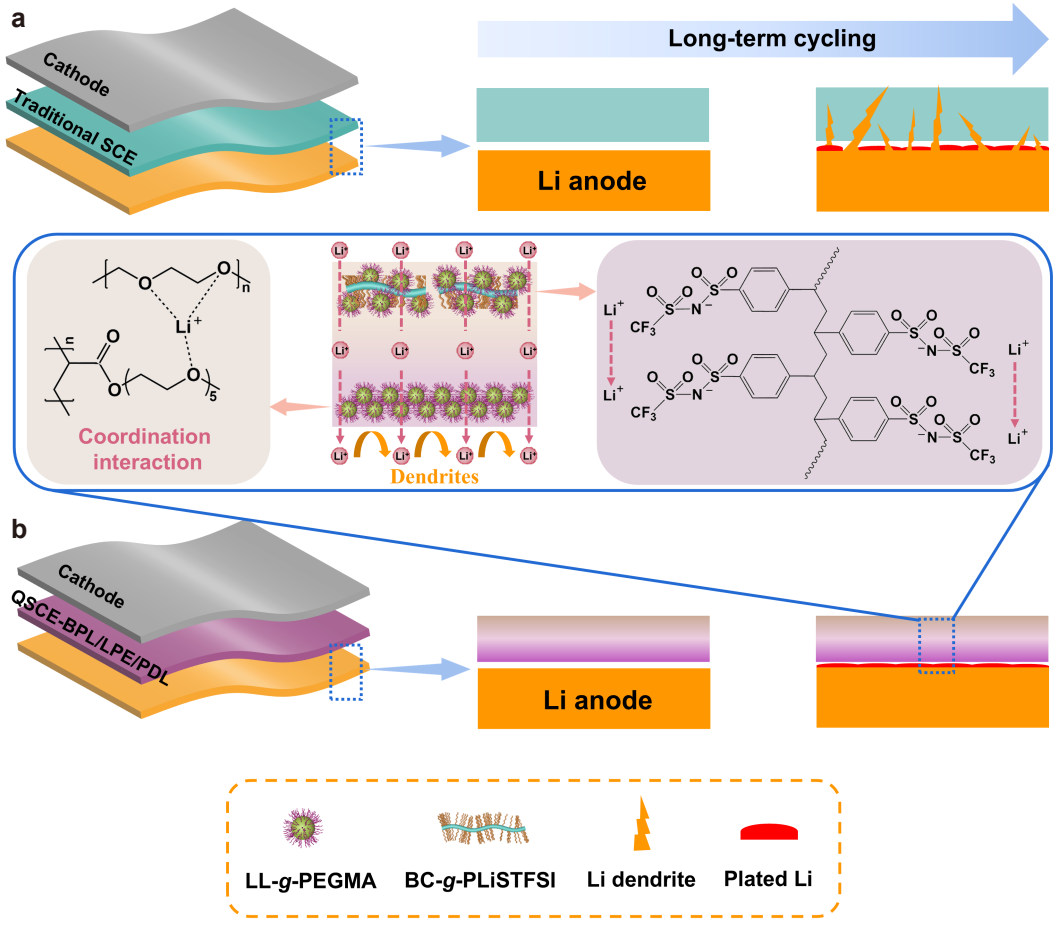

Figure 1 Schematic of lithium plating/stripping behaviors for LMBs with traditional SCE (a) and QSCE-BPL/LPE/PDL (b). Compared with traditional single-layer SCE, QSCE-BPL/LPE/PDL comprises zero-dimensional (0D) hairy nanoparticle (LL-*g*-PEGMA) and 1D molecular brush (BC-*g*-PLiSTFSI), which can enhance interfacial compatibility on the cathode side and suppress lithium dendrite growth on the anode side. The ethoxy group of hairy PEGMA side chain provides a synergistic coordination interaction with Li^+ to accelerate $LiPF_6$ dissociation. The grafted PLiSTFSI side chain could homogenize Li^+ flux, thereby improving interfacial compatibility. Moreover, the 3D porous nanonetwork structure exhibits robust mechanical performance and enables rapid Li^+ transport.

The anode-facing side typically incorporates rigid ceramic components that suppress lithium dendrite growth and promote uniform lithium deposition, whereas the cathode-facing side contains flexible polymer components that improve interfacial stability. However, current asymmetric QSCEs generally lack lithiophilic functional groups, which is unfavorable for regulating and optimizing Li^+ transport behavior. Moreover, a single asymmetric structure is insufficient to achieve multifunctional integration, resulting in limited battery performance under low-temperature conditions. Therefore, it is still a significant challenge to develop asymmetric QSCEs with hierarchical designs that can facilitate efficient Li^+ transport.

In this study, we design a novel organic–inorganic composite membrane (denoted as CM-BPL/LPE) with high interfacial compatibility and its corresponding QSCE (denoted as QSCE-BPL/LPE/PDL) (Fig. 1b). The poly(lithium 4-styrenesulfonyl-(trifluoromethylsulfonyl) imide) (PLiSTFSI) side chain on the one-dimensional (1D) molecular brush BC-*g*-PLiSTFSI (BC = bacterial cellulose) surface can achieve a single Li^+ conduction behavior, reducing the concentration polarization and improving the Li^+ transport efficiency at the organic/inorganic interface[19]. The ethoxy groups of the flexible poly(oligo(ethylene glycol) methyl ether methacrylate) (PEGMA) side chain on the zero-dimensional (0D) hairy nanoparticle LL-*g*-PEGMA (LL = $Li_{6.4}La_3Zr_{1.4}Ta_{0.6}O_{12}$) surface provide a synergistic coordination interaction with Li^+, promote lithium salt dissociation, and improve ionic conductivity, which is conducive to rapid charging/discharging at high rates[20]. The hard layer comprising LL-*g*-PEGMA contains a large number of LL ceramic substrates with high mechanical strength, which can effectively inhibit lithium dendrite growth. Even if some lithium dendrites penetrate the surface, they can be blocked by tightly stacked LL-*g*-PEGMA hairy nanoparticles in the hard layer, considerably enhancing LMB safety. Moreover, the functional polymer side chains enhance LL dispersion in BC and the interfacial compatibility between CM-BPL/LPE and poly(1,3-dioxolane). In addition, *in situ* polymerization helps reduce the electrolyte/electrode interfacial impedance. Finally, BC-*g*-PLiSTFSI and LL-*g*-PEGMA enable the formation of an asymmetric porous three-dimensional (3D) nanonetwork structure through evaporation-induced self-assembly, providing continuous and fast Li^+ transport pathways. As a result, QSCE-

BPL/LPE/PDL exhibits a high ionic conductivity of 5.44 × 10^{-4} S cm^{-1} at room temperature, and the corresponding Li|QSCE-BPL/LPE/PDL|LFP (LFP = $LiFePO_4$) cell can operate stably for 200 cycles with a high capacity retention of 94% at 0.5 C. These results indicate that the organic modification of polymer/inorganic fillers by molecular engineering strategy and the synergistic assembly using noncovalent interactions between different hybrid components can substantially improve the electrochemical performance of SCEs and facilitate the practical application of high-energy-density LMBs.

2 Experimental methods

The experimental section is available in the Electronic Supplementary Material (ESM), which is available in the online version of this article.

3 Results and discussion

Figure S1 in the ESM shows the preparation procedures of CM-BPL/LPE and QSCE-BPL/LPE/PDL. Specifically, LL-*g*-PEGMA was obtained by grafting the PEGMA side chain on the LL ceramic nanoparticle surface. BC-*g*-PLiSTFSI was synthesized by grafting the PLiSTFSI side chain from BC. Subsequently, LL-*g*-PEGMA and BC-*g*-PLiSTFSI were uniformly dispersed in *N*,*N*-dimethylformamide (DMF), and CM-BPL/LPE was prepared through self-assembly induced by natural sedimentation and interaction between building units during DMF evaporation. Finally, a novel flexible self-supporting QSCE (i.e., QSCE-BPL/LPE/PDL) with high conductivity and high thermal/mechanical stability was obtained by the *in situ* ring-opening polymerization of 1,3-dioxolane (DOL) induced by lithium hexafluorophosphate ($LiPF_6$) in the aforementioned porous CM-BPL/LPE. Figure S2 in the ESM shows the Fourier transform infrared spectroscopy (FTIR) results. Compared with commercial LL, new characteristic peaks appear at 1724, 1107, and 945 cm^{-1} for LL-*g*-PEGMA, attributable to the C=O, C–O, and C–O–C bonds, respectively[20]. After grafting PLiSTFSI from BC, BC-*g*-PLiSTFSI exhibits three new characteristic peaks at 1649, 1315, and 1196 cm^{-1}, ascribed to the stretching vibrations of C=C, S=O, and S–N, respectively[21]. FTIR results show that LL-*g*-PEGMA and BC-*g*-PLiSTFSI were successfully synthesized. According to the gel permeation chromatography traces in Fig. S3 in the ESM, the number-averaged molecular weights (M_n) of the grafted PEGMA and PLiSTFSI side chains were determined to be 2.9 × 10^4 and 3.2 × 10^4, respectively. Based on the X-ray diffraction results (Fig. S4 in the ESM), the crystal structure of the original LL ceramic nanoparticle and BC nanofiber did not change after grafting the functional side chains. As shown in the scanning electron microscopy (SEM) images of Figs. S5 and S6 in the ESM, LL-*g*-PEGMA exhibits the same nanomorphology as LL, and BC-*g*-PLiSTFSI inherits the original BC nanofiber structure. SEM elemental mapping images demonstrate that the grafted PEGMA and PLiSTFSI side chains are homogeneously dispersed, which would be conducive to regulating the uniform Li^+ transfer (Figs. S7 and S8 in the ESM).

CM-BPL/LPE is prepared by the evaporation-induced self-assembly of BC-*g*-PLiSTFSI and LL-*g*-PEGMA with a mass ratio of 1:2 (Fig. 2a). CM-BPL/LPE has an asymmetric and porous structure, where the top of CM-BPL/LPE (CM-BPL/LPE-t) mainly comprises LL-*g*-PEGMA and BC-*g*-PLiSTFSI, whereas the bottom of CM-BPL/LPE (CM-BPL/LPE-b) is primarily formed by LL-*g*-PEGMA stack-

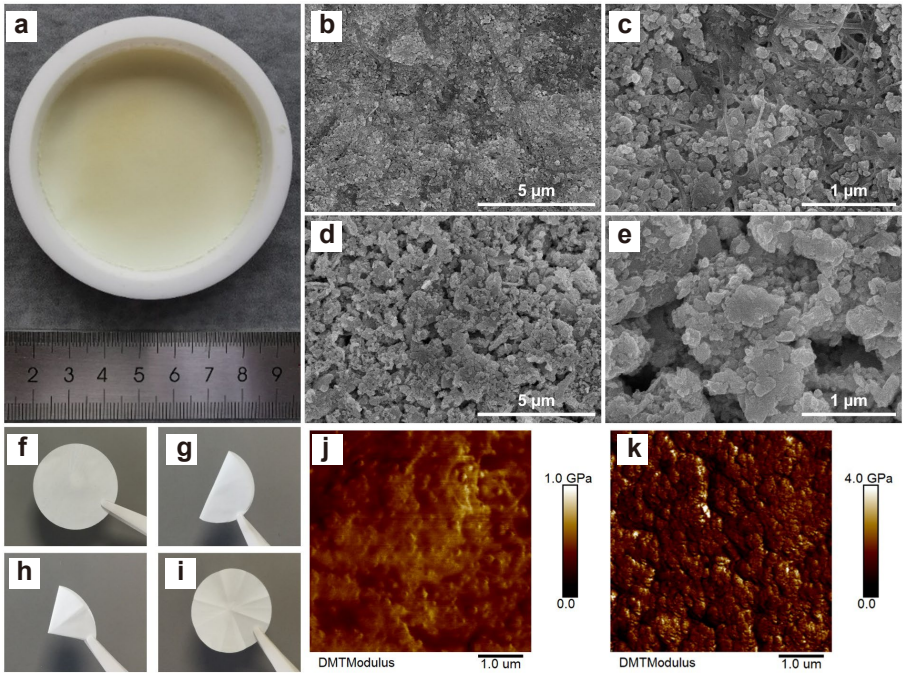

Figure 2 (a) Digital photo of a large piece of CM-BPL/LPE. Top-view (b, c) and bottom-view (d, e) SEM images of CM-BPL/LPE at different magnifications. Digital photos of QSCE-BPL/LPE/PDL (f), and its bending (g) and folding (h). (i) Digital photo of QSCE-BPL/LPE/PDL after bending and folding 100 times. AFM Young's modulus mappings of QSCE-BPL/LPE/PDL-t (j) and QSCE-BPL/LPE/PDL-b (k).

ing (Figs. 2b–2e). Control samples are prepared by adjusting the ratio of different hybrid components, including the composite membranes (CM-2BPL/1LPE, CM-1BPL/1LPE, CM-1BPL/2LL, CM-1BC/2LPE, and CM-1BC/2LL). As shown in Fig. S9 in the ESM, CM-1BPL/1LPE and CM-2BPL/1LPE exhibit asymmetric network structures. When the mass ratio is 1:1, a small amount of BC-*g*-PLiSTFSI can be observed on the CM-BPL/LPE-b surface, indicating that the lower content of LL-*g*-PEGMA is insufficient to effectively cover the underside of the composite membrane. Meanwhile, when the mass ratio is increased to 2:1, only a small amount of LL-*g*-PEGMA is observed on the CM-BPL/LPE-t surface, whereas the content of BC-*g*-PLiSTFSI on the CM-BPL/LPE-b surface is further increased.

Notably, CM-BPL/LPE-V, which is obtained by vacuum filtration, exhibits an asymmetric structure with severe LL nanoparticle agglomeration, suggesting that the membrane formation method considerably affects the microstructure of CM-BPL/LPE (Fig. S10 in the ESM). CM-1BC/2LL also displays severe LL nanoparticle agglomeration, which is not conducive to Li^+ conduction and interfacial contact (Fig. S11 in the ESM). Furthermore, compared with CM-1BC/2LL, CM-1BPL/2LL (BC-*g*-PLiSTFSI with unmodified LL) and CM-1BC/2LPE (unmodified BC with LL-*g*-PEGMA) show marginally improved nanoparticle dispersion (Fig. S12 in the ESM). Nevertheless, nanoparticle agglomerates remain evident in both composite membranes. These results indicate that the interaction between BC-*g*-PLiSTFSI and LL-*g*-PEGMA functional side chains could considerably alleviate nanoparticle agglomeration.

To investigate the wettability of precursor solutions containing ester-based electrolytes and DOL, the contact angle was tested for pure BC membrane, commercial polypropylene (PP) separator, and CM-BPL/LPE. As shown in Fig. S13 in the ESM, the contact angles of CM-BPL/LPE-t and CM-BPL/LPE-b are 9° and 7°, respectively, which are much smaller than those of the BC membrane (27°) and PP separator (42°). Owing to its nonpolar substrate and low surface energy, the PP separator apparently exhibits the largest contact angle. Meanwhile, the precursor solution wettability of the PP separator is worse than that of the BC membrane, which contains hydroxyl functional groups. CM-BPL/LPE demonstrates the best affinity with the precursor solution because abundant stacked pore structures can be formed on CM-BPL/LPE-t and CM-BPL/LPE-b during the solvent evaporation-induced self-assembly process. The well-developed pores play a pivotal role in providing fast Li^+ pathways. In addition, the introduction of abundant hairy PLiSTFSI and PEGMA side chains can facilitate precursor solution infiltration and reduce interfacial impedance, and further improve Li^+ transport efficiency. The Young's moduli of CM-BPL/LPE-t and CM-BPL/LPE-b are 1.28 and 3.17 GPa, respectively, exhibiting a noticeable difference (Fig. S14 in the ESM). This is because CM-BPL/LPE-b primarily comprises LL-*g*-PEGMA network units, whose rigid structure enhances its mechanical strength. As shown in Fig. S15 in the ESM, the force–depth curves suggest that the elastic moduli of CM-BPL/LPE-t and CM-BPL/LPE-b are up to 0.61 and 1.58 GPa, respectively, which are both much higher than that of the BC membrane (0.18 GPa).

After CM-BPL/LPE absorbs the precursor solution comprising DOL and commercial ester-based LE (2 mol/L $LiPF_6$ in ethylene carbonate/dimethyl carbonate/diethyl carbonate with a volume ratio of 1:1:1) with a volume ratio of 9:1, the corresponding QSCE (QSCE-BPL/LPE/PDL) is obtained by *in situ* ring-opening polymerization. We investigated the effect of different $LiPF_6$ concentrations and the DOL volume fractions of the precursor solutions on the *in situ* gelation process (Fig. S16a in the ESM). It is difficult to form gels with a low concentration of $LiPF_6$ (0.1 mol/L) and a high volume fraction of DOL (90%) within 12 h at room temperature. Meanwhile, under the conditions of $LiPF_6$ (0.5 mol/L) and DOL (50%), $LiPF_6$ (1 mol/L) and DOL (50%), and $LiPF_6$ (0.2 mol/L) and DOL (90%), DOL monomers can polymerize to yield an SE within 12 h. However, only the precursor solution containing $LiPF_6$ (0.2 mol/L) and DOL (90%) can form a gel that shows no obvious fluidity after being inverted for 1 h; thus, this precursor solution proportion is used in subsequent SE preparation. As shown in Fig. S16b in the ESM, the corresponding mechanism can be summarized as the cationic ring-opening polymerization of DOL by $LiPF_6$[22].

QSCE-BPL/LPE/PDL demonstrates flexible self-supporting characteristics, which can retain structural integrity even after repeated bending and folding 100 times (Figs. 2f–2i). Other control QSCEs (QSCE-2BPL/1LPE/PDL, QSCE-1BPL/1LPE/PDL, and QSCE-1BC/2LL/PDL) and quasi-solid-state polymer electrolytes (QSPE-BC/PDL and QSPE-PP/PDL) are also prepared. Atomic force microscopy (AFM) measurements reveal that QSCE-BPL/LPE/PDL possesses mechanical asymmetry, with Young's moduli of 0.42 and 1.33 GPa for its top surface (QSCE-BPL/LPE/PDL-t) and bottom surface (QSCE-BPL/LPE/PDL-b), respectively (Figs. 2j and 2k). For comparison, the Young's modulus of QSPE-BC/PDL was measured to be 1.10 GPa under identical conditions (Fig. S17 in the ESM). In addition, the elastic modulus of QSCE-BPL/LPE/PDL remains at 0.16 GPa (QSCE-BPL/LPE/PDL-t) and 0.2 GPa (QSCE-BPL/LPE/PDL-b), which are higher than that of QSPE-BC/PDL (0.11 GPa; Fig. S18 in the ESM). Because of its unique asymmetric structure, QSCE-BPL/LPE/PDL not only ensures flexible interfacial contact with the cathode but also effectively inhibits the penetration of lithium dendrites at the anode side. To evaluate thermal stability, thermal shrinkage test of QSCE-BPL/LPE/PDL and QSPE-PP/PDL was conducted by placing both samples in an oven at different temperatures for 0.5 h. As shown in Fig. S19 in the ESM, QSPE-PP/PDL begins to undergo notable size self-shrinkage at 100 °C and is completely curled at 150 °C. Meanwhile, QSCE-BPL/LPE/PDL exhibits almost no visible shrinkage during the heating process (25–150 °C), demonstrating that QSCE-BPL/LPE/PDL can greatly keep macroscopic morphological integrity and reduce the short-circuit risk of LMBs at high temperatures.

QSCE-BPL/LPE/PDL is as thin as 19 μm (Fig. S20 in the ESM). Such an ultrathin QSCE can considerably shorten Li^+ transport pathways and increase the energy density of LMBs. The ionic conductivity of QSCE-BPL/LPE/PDL and the control samples was measured using electrochemical impedance spectroscopy (EIS) tests at room temperature (Fig. 3a). QSCE-BPL/LPE/PDL exhibits a higher ionic

conductivity (5.44×10^{-4} S cm^{-1}) than QSCE-1BPL/1LPE/PDL (1.04×10^{-4} S cm^{-1}), QSCE-2BPL/1LPE/PDL (1.61×10^{-4} S cm^{-1}), QSPE-BC/PDL (0.25×10^{-4} S cm^{-1}), and QSCE-1BC/2LL/PDL (0.77×10^{-4} S cm^{-1}). These results suggest that the PLiSTFSI and PEGMA side chains enhance the ionic conductivity. To gain deeper insight into the Li^+ transport kinetics, the activation energy (E_a) for ionic conduction was calculated based on the temperature-dependent conductivity data (Fig. 3b and Fig. S21 in the ESM). The resulting E_a for QSCE-BPL/LPE/PDL is as low as 5.7 kJ/mol, which is substantially lower than that of QSPE-BC/PDL (24.9 kJ/mol). This result demonstrates that efficient Li^+ diffusion with a low ion migration barrier is achieved in QSCE-BPL/LPE/PDL. Remarkably, QSCE-BPL/LPE/PDL maintains a high ionic conductivity of 3.75×10^{-4} S cm^{-1} at −10 °C, indicating that the ultrathin electrolyte has potential application in low-temperature environments (Fig. S22 in the ESM). Benefiting from the synergistic effect of the unique asymmetric structure, interaction between different-dimensional functional components, and *in situ* cationic ring-opening polymerization, QSCE-BPL/LPE/PDL exhibits excellent superiority in terms of thickness and ionic conductivity over most reported SEs (e.g., 4.45×10^{-4} S cm^{-1} at 30 °C with 19 μm for BPMF-QSPE[23], 3.51×10^{-4} S cm^{-1} at 30 °C with 26 μm for R-ANF-MOF[24], and 1.0×10^{-4} S cm^{-1} at 30 °C with 35 μm for PL-LSLOH[25]) (Fig. 3c and Table S1 in the ESM). The linear sweep voltammetry (LSV) curves reveal that QSCE-BPL/LPE/PDL possesses superior electrochemical stability, withstanding up to ~4.9 V vs. Li^+/Li, which is higher than that of QSPE-BC/PDL (~4.7 V; Fig. 3d).

The Li^+ transference number (t_{Li^+}) is tested to quantitatively evaluate the Li^+ migration characteristics of various

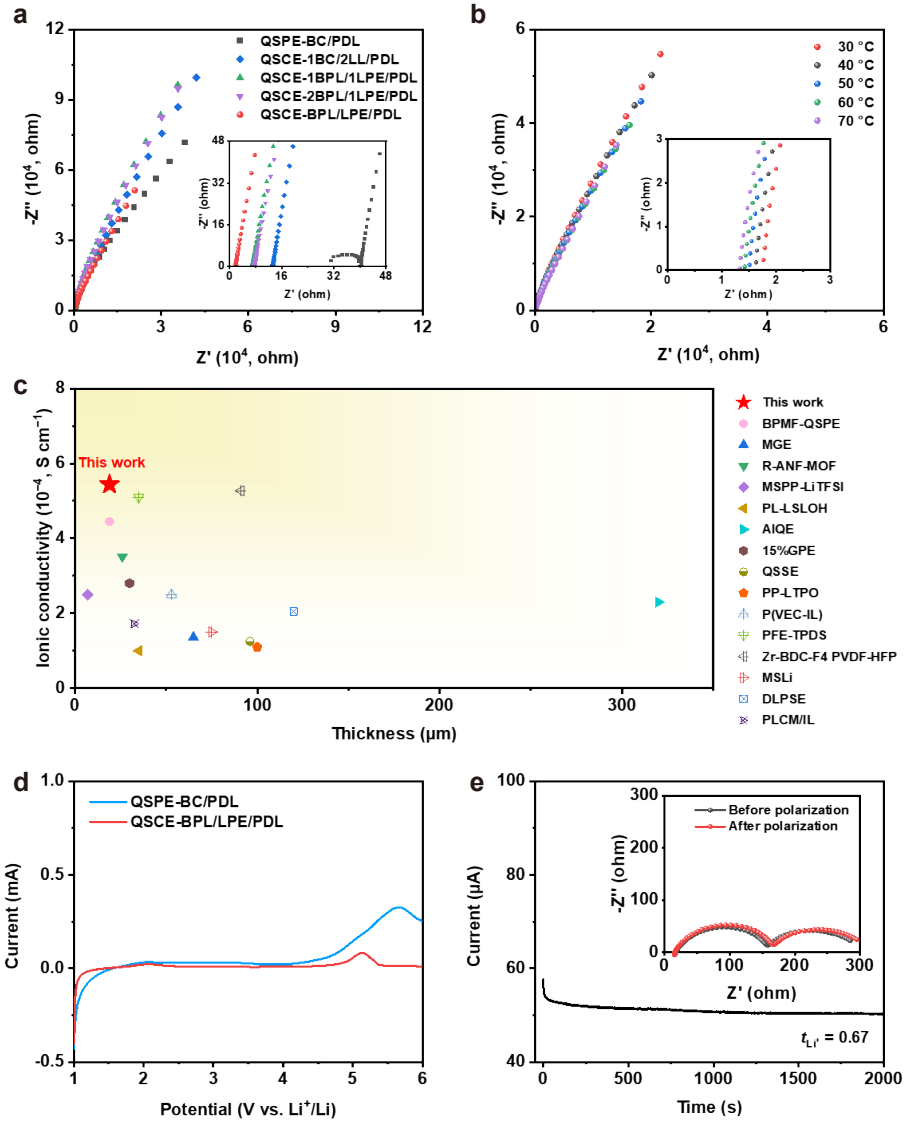

Figure 3 (a) Nyquist plots of QSPE-BC/PDL, QSCE-1BC/2LL/PDL, QSCE-1BPL/1LPE/PDL, QSCE-2BPL/1LPE/PDL, and QSCE-BPL/LPE/PDL at room temperature. (b) Nyquist plots of QSCE-BPL/LPE/PDL at various temperatures from 30 to 70 °C. (c) Comparison of thickness and ionic conductivity between QSCE-BPL/LPE/PDL and reported SEs. (d) LSV curves of QSPE-BC/PDL and QSCE-BPL/LPE/PDL at a scan rate of 5 mV s^{-1}. (e) Chronoamperometry profile of Li|QSCE-BPL/LPE/PDL|Li cell at 10 mV polarization (inset: Nyquist plots before and after polarization).

quasi-solid-state electrolytes. Benefiting from the single Li^+ conducting ability of the PLiSTFSI side chain and fast Li^+ conduction of the LL ceramic nanoparticle, QSCE-BPL/LPE/PDL has a high t_{Li^+} of 0.67, which is much higher than those of QSCE-1BC/2LL/PDL (0.41) and QSPE-BC/PDL (0.35) (Fig. 3e and Fig. S23 in the ESM). In addition, the t_{Li^+} of QSCE-BPL/LPE/PDL is higher than those of reported single-layer SEs (e.g., 0.56 for fluorinated polymer[26] and 0.65 for PDOL-TFEP[27]) and multi-layer SEs (0.23 for m-PPL[28] and 0.60 for PLM[29]) (Fig. S24 in the ESM). The high t_{Li^+} of QSCE-BPL/LPE/PDL helps reduce the Li^+ concentration gradient at the QSCE/electrode interface. Such excellent ionic conductivity and high t_{Li^+} could be ascribed to *in situ* ring-opening polymerization and the unique asymmetric structure comprising BC-*g*-PLiSTFSI and LL-*g*-PEGMA. On the one hand, the 3D interconnected porous structure formed by the stacking of different hybrid components can reduce Li^+ transport pathways, facilitating rapid Li^+ transport. On the other hand, similar to the reported single Li^+ conducting electrolytes, the grafted PLiSTFSI side chain with a single Li^+ migration characteristic can improve the Li^+ transport efficiency and homogenize Li^+ flux. In addition, the PEGMA side chain can effectively enhance the interfacial compatibility between hybrid components and considerably promote $LiPF_6$ dissociation.

Owing to its notable physicochemical advantages, QSCE-BPL/LPE/PDL is expected to regulate lithium deposition and inhibit lithium dendrite growth. As shown in Fig. 4a, the Li/Li symmetric cell with QSCE-BPL/LPE/PDL exhibits steady and low lithium plating/stripping overpotentials of 16, 29, 43, 70, and 148 mV at current densities of 0.1, 0.2, 0.3, 0.5, and 1 mA cm^{-2}, respectively, demonstrating fast Li^+ transport kinetics and excellent interfacial properties. Meanwhile, the Li/Li symmetric cell with QSPE-BC/PDL delivers much larger overpotentials with severely fluctuating plating/stripping voltage profiles, and this cell fails at 0.5 mA cm^{-2}. Li|QSCE-BPL/LPE/PDL|Li exhibits superior cycling stability with stable voltage plateaus for 700 h at certain current densities (e.g., 0.2 and 0.5 mA cm^{-2}) compared with Li|QSPE-BC/PDL|Li, Li|QSCE-1BC/2LL/PDL|Li, Li|QSCE-2BPL/1LPE/PDL|Li, and Li|QSCE-1BPL/1LPE/PDL|Li (Figs. 4b, 4c, and Fig. S25 in the ESM). The nanomorphologies of lithium metals from Li/Li cells after 50 cycles with different electrolytes are observed by SEM (Figs. 4d–4i). Compared with the smooth surface of the original lithium foil, the lithium metal from the cycled Li/Li cell with QSPE-BC/PDL demonstrates obvious roughness and porosity, attributable to the formation of a large amount of mossy lithium by inhomogeneous lithium plating/stripping. Meanwhile, the lithium metal from Li|QSCE-BPL/LPE/PDL|Li cell remains compact and smooth without distinct lithium dendrites. To further evaluate the interfacial stability, EIS was conducted on

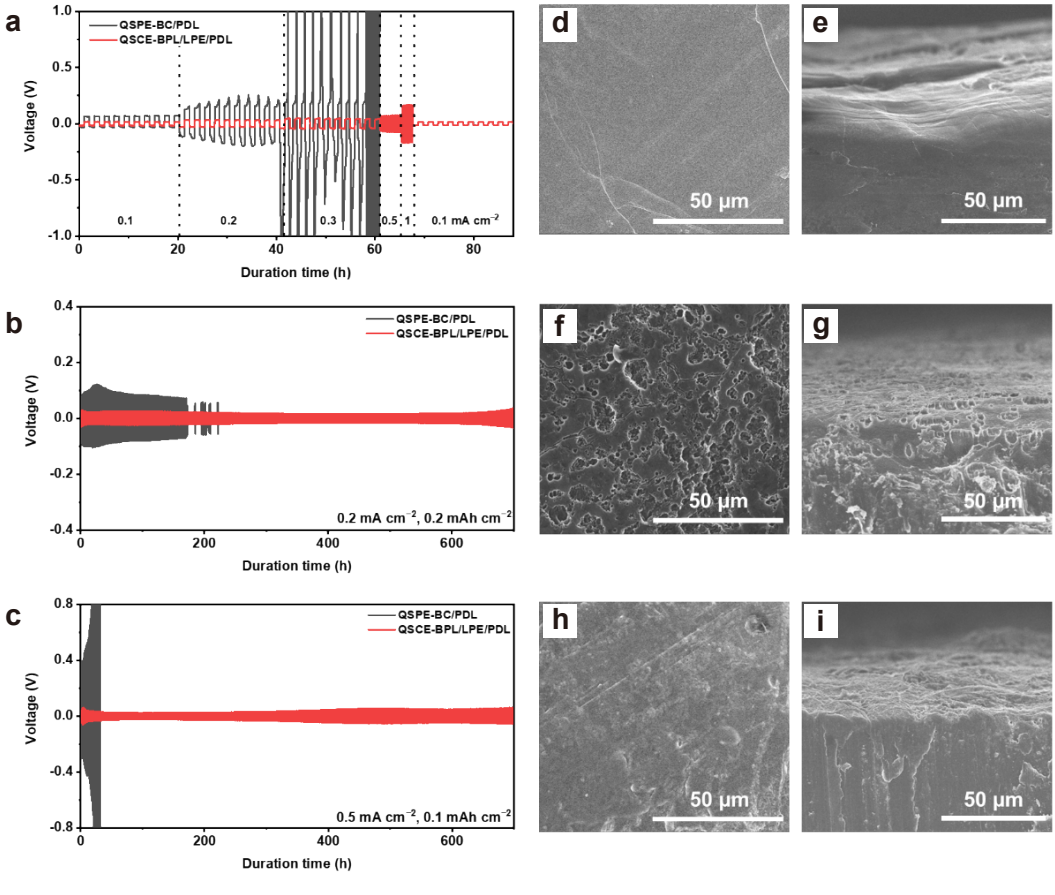

Figure 4 (a) Voltage–time profiles of Li/Li cells with QSPE-BC/PDL and QSCE-BPL/LPE/PDL at various current densities. Voltage–time profiles of symmetric Li/Li cells with QSPE-BC/PDL and QSCE-BPL/LPE/PDL at 0.2 mA cm^{-2} and 0.2 mAh cm^{-2} (b); and at 0.5 mA cm^{-2} and 0.1 mAh cm^{-2} (c). Top-view and cross-sectional SEM images of fresh lithium metal (d, e) and lithium metals from cycled Li/Li cells with QSPE-BC/PDL (f, g) and QSCE-BPL/LPE/PDL (h, i).

Li/Li symmetric cells assembled with different electrolytes. As shown in Fig. S26 in the ESM, the Nyquist plot of the Li/Li cell with QSCE-BPL/LPE/PDL exhibits a substantially smaller semicircle than those of the Li/Li cells with QSPE-BC/PDL and QSPE-PP/PDL, indicating much lower interfacial resistance. This result confirms that the asymmetric QSCE-BPL/LPE/PDL facilitates the formation of a stable solid-electrolyte interphase layer, consistent with its excellent cycling performance and dendrite-free lithium deposition.

To demonstrate the potential of QSCE-BPL/LPE/PDL in practical LMBs, the electrochemical performance of Li/LFP cells with different quasi-solid-state electrolytes is also evaluated. As shown in Fig. 5a, the Li|QSCE-BPL/LPE/PDL|LFP cell delivers discharge capacities of 143, 136, 129, 118, 107, and 89 mAh g^{-1} at 0.2, 0.5, 1, 2, 3, and 5 C, respectively, and recovers to 139 mAh g^{-1} when the current density returns to 0.2 C, indicating superior rate performance compared with the Li|QSPE-PP/PDL|LFP and Li|QSPE-BC/PDL|LFP cells. The charge/discharge profiles of Li|QSCE-BPL/LPE/PDL|LFP cell at various rates show stable voltage plateaus, suggesting that no side reaction occurs during cycling (Fig. 5b). Benefiting from the excellent Li^+ transport kinetics of QSCE-BPL/LPE/PDL, the Li|QSCE-BPL/LPE/PDL|LFP cell exhibits decreased interfacial charge transfer impedance compared with the Li|QSPE-BC/PDL|LFP and Li|QSPE-PP/PDL|LFP cells (Fig. 5c). Compared with other

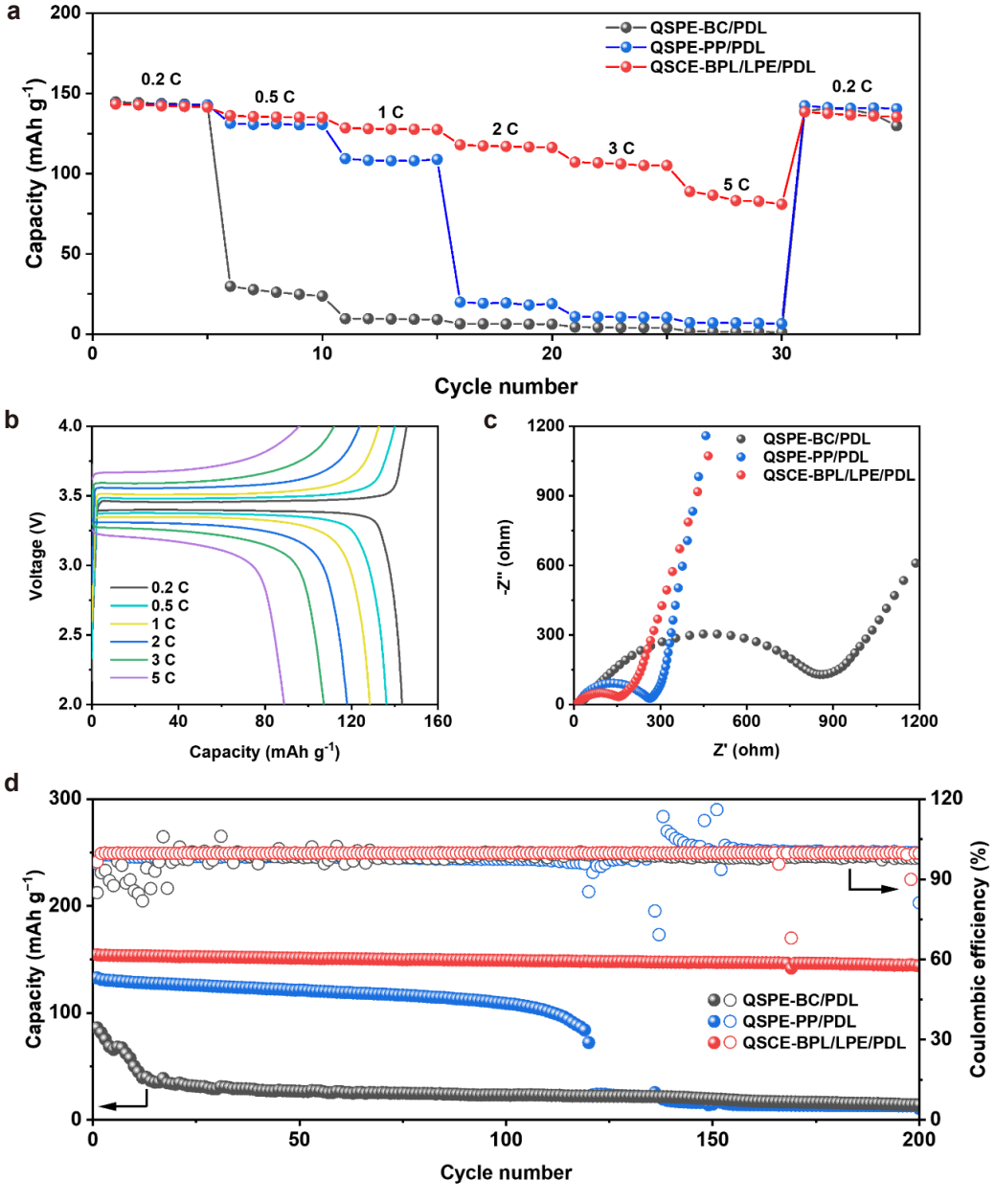

Figure 5 (a) Rate performance of Li/LFP cells with QSPE-BC/PDL, QSPE-PP/PDL, and QSCE-BPL/LPE/PDL. (b) Initial charge/discharge profiles of Li/LFP cell with QSCE-BPL/LPE/PDL at various rates. (c) Nyquist plots of Li/LFP cells with QSPE-BC/PDL, QSPE-PP/PDL, and QSCE-BPL/LPE/PDL. (d) Cycling performance of Li/LFP cells with QSPE-BC/PDL, QSPE-PP/PDL, and QSCE-BPL/LPE/PDL at 0.5 C.

control samples, Li/LFP cells with QSCE-BPL/LPE/PDL also exhibit much better cycling performance. The Li|QSCE-BPL/LPE/PDL|LFP cell sustains 94% of the initial discharge capacity after 200 cycles at 0.5 C, which is superior to those of Li/LFP cells with QSPE-BC/PDL (16%) and QSPE-PP/PDL (8%) (Fig. 5d).

To further demonstrate the critical role of the asymmetric architecture, we fabricated a reversed configuration (QSCE-BPL/LPE/PDL-R) in which the rigid LL-*g*-PEGMA-rich hard layer faced the cathode and the soft composite layer faced the lithium anode. The cycling performance of Li/LFP cell with QSCE-BPL/LPE/PDL-R at 0.5 C is shown in Fig. S27 in the ESM. The initial discharge capacity is 141 mAh g^{-1}, but the capacity declines to 100 mAh g^{-1} after 200 cycles, corresponding to a capacity retention of only 71%. The poor stability of the reversed cell indicates that the mechanically weaker composite layer on the anode side fails to suppress lithium dendrite penetration, resulting in dead lithium formation and rapid capacity decay. Therefore, the original design is essential for simultaneously suppressing dendrites and maintaining intimate cathode interfacial contact.

By replacing LFP with other commercial materials [e.g., $Li_4Ti_5O_{12}$ (LTO)], the resulting Li|QSCE-BPL/LPE/PDL|LTO cell still delivers a high initial discharge capacity of 159 mAh g^{-1} with an excellent capacity retention of 92% over 500 cycles at 1 C, whereas Li|QSPE-PP/PDL|LTO and Li|QSPE-BC/PDL|LTO cells display a much lower discharge capacity (Fig. S28 in the ESM). Notably, the Li/LTO cell with QSCE-BPL/LPE/PDL also maintains good cycling stability even at −10 °C (146 mAh g^{-1} after 500 cycles; Fig. S29 in the ESM). These results suggest that the ultrathin QSCE-BPL/LPE/PDL exhibits high Li^+ transfer efficiency and fast Li^+ transport dynamics, and considerably enhances the rate and cycling performances of LMBs.

4 Conclusion

In summary, we developed an effective strategy for preparing a novel class of asymmetric QSCEs (QSCE-BPL/LPE/PDL) via an evaporation-induced self-assembly of low-dimensional functional hybrid components combined with *in situ* cationic ring-opening polymerization. Benefiting from PLiSTFSI side-chain-homogenized Li^+ flux, PEGMA side-chain-improved Li^+ transport efficiency, and 3D porous structure-shortened Li^+ transport pathways, QSCE-BPL/LPE/PDL exhibits satisfactory electrochemical properties for LMBs, including excellent ionic conductivity at an ultrathin thickness, a high Li^+ transference number, robust mechanical performance, and excellent cycling stability toward the lithium anode. This study demonstrates that designing unique asymmetric QSCEs via molecular engineering is a promising research direction to fundamentally promote Li^+ conduction and stabilize the lithium anode, providing a viable strategy for the practical application of high-performance solid-state LMBs.

Acknowledgements

None.

Author contribution statement

D.W. supervised the research. Y.C. and D.W. conceived the concept. S.L. designed the project and synthesized the materials. S.L., Y.C., G.Y., D.M., and R.L. performed the material characterizations and electrochemical tests. S.L., Y.C., and D.W. wrote the manuscript. All the authors discussed the results, commented on and approved the manuscript.

Data availability

The data that support the findings of this study are included in the article and the supplementary materials.

Declaration of competing interest

Dingcai Wu is an Associate Editor of this journal, but he was not involved in the peer review or decision of this article. All the other contributing authors report no conflicts of interest in this work.

Funding

This work was supported by the National Key Research and Development Program of China (Grant No. 2021YFF0500600), the National Natural Science Foundation of China (Grant No. 52533009), the Guangdong Major Project of Basic and Applied Basic Research (Grant No. 2023B0303000025), the Natural Science Foundation of Guangdong (Grant Nos. 2024B1515020023 and 2023A1515030160), the Fundamental Research Funds for the Central Universities, Sun Yat-sen University (Grant Nos. 23yxqntd002 and 23lgbj004), the Science and Technology Program of Guangzhou (Grant No. 2024A04J10003), and the Guangdong Basic Research Center of Excellence for Functional Molecular Engineering. The authors thank the Instrumental Analysis & Research Center, Sun Yat-sen University.

Use of AI statement

None.

Electronic Supplementary Material: Supplementary material (the experimental methods) is available in the online version of this article at https://doi.org/10.26599/EMD.2026.9370095

References

[1] Wu, F. X., Maier, J., Yu, Y. (2020). Guidelines and trends for next-generation rechargeable lithium and lithium-ion batteries. *Chem. Soc. Rev.* 49, 1569–1614.

[2] Choi, J. W., Aurbach, D. (2016). Promise and reality of post-lithium-ion batteries with high energy densities. *Nat. Rev. Mater.* 1, 16013.

[3] Cui, Y., Shi, S. S., Lu, C. K., Cai, Z. Q., Zhang, G. B., Li, L., Yang, T., Liu, T., Liu, Q. X., Lin, X. D. (2026). In-situ coupled macromolecular bridge enables all-solid-state lithium metal batteries capable of extremely high temperature operation. *Carbon Neutral.* 5, e70099.

[4] Wu, W. Y., Luo, W., Huang, Y. H. (2023). Less is more: a perspective on thinning lithium metal towards high-energy-density

rechargeable lithium batteries. *Chem. Soc. Rev.* 52, 2553–2572.
[5] Yao, N., Chen, X., Fu, Z. H., Zhang, Q. (2022). Applying classical, *ab initio*, and machine-learning molecular dynamics simulations to the liquid electrolyte for rechargeable batteries. *Chem. Rev.* 122, 10970–11021.
[6] Jiang, F. N., Cheng, X. B., Yang, S. J., Xie, J., Yuan, H., Liu, L., Huang, J. Q., Zhang, Q. (2023). Thermoresponsive electrolytes for safe lithium-metal batteries. *Adv. Mater.* 35, 2209114.
[7] Zhu, G. R., Zhang, Q., Liu, Q. S., Bai, Q. Y., Quan, Y. Z., Gao, Y., Wu, G., Wang, Y. Z. (2023). Non-flammable solvent-free liquid polymer electrolyte for lithium metal batteries. *Nat. Commun.* 14, 4617.
[8] Lu, C. K., Geng, N. N., Sun, Y. Q., Yang, T., Yi, Y., Zhang, G. B., Su, C., Lin, X. D., Cui, Y. (2026). Advances in silane-bridging engineering for stable lithium metal batteries. *J. Colloid Interface Sci.* 704, 139441.
[9] Chen, L. K., Gu, T., Mi, J. S., Li, Y. H., Yang, K., Ma, J. B., An, X. F., Jiang, Y. Y., Zhang, D. F., Cheng, X., et al. (2025). Homogeneous polymer-ionic solvate electrolyte with weak dipole-dipole interaction enabling long cycling pouch lithium metal battery. *Nat. Commun.* 16, 3517.
[10] Yoon, K., Lee, S., Oh, K., Kang, K. (2022). Challenges and strategies towards practically feasible solid-state lithium metal batteries. *Adv. Mater.* 34, 2104666.
[11] Chen, R. S., Li, Q. H., Yu, X. Q., Chen, L. Q., Li, H. (2020). Approaching practically accessible solid-state batteries: stability issues related to solid electrolytes and interfaces. *Chem. Rev.* 120, 6820–6877.
[12] Liu, S. L., Liu, W. Y., Ba, D. L., Zhao, Y. Z., Ye, Y. H., Li, Y. Y., Liu, J. P. (2023). Filler-integrated composite polymer electrolyte for solid-state lithium batteries. *Adv. Mater.* 35, 2110423.
[13] Zheng, Y., Yao, Y. Z., Ou, J. H., Li, M., Luo, D., Dou, H. Z., Li, Z. Q., Amine, K., Yu, A. P., Chen, Z. W. (2020). A review of composite solid-state electrolytes for lithium batteries: fundamentals, key materials and advanced structures. *Chem. Soc. Rev.* 49, 8790–8839.
[14] Fan, L. Z., He, H. C., Nan, C. W. (2021). Tailoring inorganic–polymer composites for the mass production of solid-state batteries. *Nat. Rev. Mater.* 6, 1003–1019.
[15] Li, S., Zhang, S. Q., Shen, L., Liu, Q., Ma, J. B., Lv, W., He, Y. B., Yang, Q. H. (2020). Progress and perspective of ceramic/polymer composite solid electrolytes for lithium batteries. *Adv. Sci.* 7, 1903088.
[16] Mi, J. S., Yang, J., Chen, L. K., Cui, W. T., Li, Y. H., An, X. F., Ma, J. B., Yang, K., Xie, Y. S., Biao, J., et al. (2025). A ductile solid electrolyte interphase for solid-state batteries. *Nature* 647, 86–92.
[17] Liu, Z. X., Wu, F., Chen, R. J., Li, L. (2025). Bifacial leaf-inspired tailored design for asymmetric quasi-solid-state electrolytes enabling high-performance lithium metal batteries. *Energy Storage Mater.* 81, 104511.
[18] Du, G. Y., Chen, D. C., Muhtar, D., Lai, H., Cao, J. Q., Xie, F. Y., Yang, S., Lu, X. (2026). A universal design of quasi-solid-state battery with asymmetric composite electrolyte. *Energy Storage Mater.* 84, 104776.
[19] Zhou, M. H., Liu, R. L., Jia, D. Y., Cui, Y., Liu, Q. T., Liu, S. H., Wu, D. C. (2021). Ultrathin yet robust single lithium-ion conducting quasi-solid-state polymer-brush electrolytes enable ultralong-life and dendrite-free lithium-metal batteries. *Adv. Mater.* 33, 2100943.
[20] Li, S. M., Huang, J. L., Cui, Y., Liu, S. H., Chen, Z. R., Huang, W., Li, C. F., Liu, R. L., Fu, R. W., Wu, D. C. (2022). A robust all-organic protective layer towards ultrahigh-rate and large-capacity Li metal anodes. *Nat. Nanotechnol.* 17, 613–621.
[21] Cao, C., Li, Y., Feng, Y. Y., Long, P., An, H. R., Qin, C. Q., Han, J. K., Li, S. W., Feng, W. (2017). A sulfonimide-based alternating copolymer as a single-ion polymer electrolyte for high-performance lithium-ion batteries. *J. Mater. Chem. A* 5, 22519–22526.
[22] Liu, F. Q., Wang, W. P., Yin, Y. X., Zhang, S. F., Shi, J. L., Wang, L., Zhang, X. D., Zheng, Y., Zhou, J. J., Li, L., et al. (2018). Upgrading traditional liquid electrolyte via *in situ* gelation for future lithium metal batteries. *Sci. Adv.* 4, eaat5383.
[23] Li, C. P., Zhong, Y., Liao, R. F., Yi, T., Zhou, M. H., Liu, R. L., Liu, S. H., Wu, D. C. (2025). Robust and antioxidative quasi-solid-state polymer electrolytes for long-cycling 4.6 V lithium metal batteries. *Adv. Mater.* 37, 2500142.
[24] Gu, J. P., Dong, C. X., Zhu, Y. X., Liu, H. Y., Ji, J., Yu, Y. K., Ma, C. N., Zhou, C., Mai, L. Q., Xu, X. (2025). Constructing matching interfaces by amorphous engineering for enhanced lithium ion transport in quasi-solid-state lithium–iodine batteries. *Angew. Chem. Int. Ed.* 64, e202507184.
[25] Liu, H. W., Zhao, L. Q., Jiang, P. F., Sun, X., Hester, J., Zhang, S. Q., Guan, D. Q., Shao, Z. P. (2026). $La(OH)_3$-based lithium ionic conductor for quasi-solid-state lithium metal batteries. *Adv. Mater.* 38, e16709.
[26] Li, Z. Y., Li, W. M., Li, Z., Fu, J. L., Chen, Q., Yang, H., Guo, X. (2025). Fluorine-oxygen co-coordination of lithium in fluorinated polymers for broad temperature quasi-solid-state batteries. *Nat. Commun.* 16, 9265.
[27] Wang, Z. L., Shen, L. Y., Ma, Y. L., Law, H. M., Xu, S. J., Bi, Y. X., Robson, M. J., Wang, Y. H., Gröschel, A., Chen, Q., et al. (2025). Enthalpy-driven molecular engineering enables high-performance quasi-solid-state electrolytes for long life lithium metal batteries. *Adv. Mater.* 37, 2419335.
[28] Wang, Z. Y., Shen, L., Deng, S. G., Cui, P., Yao, X. Y. (2021). 10 μm-thick high-strength solid polymer electrolytes with excellent interface compatibility for flexible all-solid-state lithium-metal batteries. *Adv. Mater.* 33, 2100353.
[29] Zhang, Z., Gou, J. R., Cui, K. X., Zhang, X., Yao, Y. J., Wang, S. Q., Wang, H. H. (2024). 12.6 μm-thick asymmetric composite electrolyte with superior interfacial stability for solid-state lithium-metal batteries. *Nano-Micro Lett.* 16, 181.